

Partially sintered copper–ceria as excellent catalyst for the high-temperature reverse water gas shift reaction

Hao-Xin Liu ^{1,4}, Shan-Qing Li ^{2,4}, Wei-Wei Wang ¹, Wen-Zhu Yu ¹, Wu-Jun Zhang ³, Chao Ma ³✉ & Chun-Jiang Jia ¹✉

For high-temperature catalytic reaction, it is of significant importance and challenge to construct stable active sites in catalysts. Herein, we report the construction of sufficient and stable copper clusters in the copper–ceria catalyst with high Cu loading (15 wt.%) for the high-temperature reverse water gas shift (RWGS) reaction. Under very harsh working conditions, the ceria nanorods suffered a partial sintering, on which the 2D and 3D copper clusters were formed. This partially sintered catalyst exhibits unmatched activity and excellent durability at high temperature. The interaction between the copper and ceria ensures the copper clusters stably anchored on the surface of ceria. Abundant in situ generated and consumed surface oxygen vacancies form synergistic effect with adjacent copper clusters to promote the reaction process. This work investigates the structure-function relation of the catalyst with sintered and inhomogeneous structure and explores the potential application of the sintered catalyst in C1 chemistry.

¹Key Laboratory for Colloid and Interface Chemistry, Key Laboratory of Special Aggregated Materials, School of Chemistry and Chemical Engineering, Shandong University, Jinan 250100, China. ²Key Laboratory of Micro-Nano Powder and Advanced Energy Materials of Anhui Higher Education Institutes, Chizhou University, Chizhou 247000, China. ³College of Materials Science and Engineering, Hunan University, Changsha 410082, China. ⁴These authors contributed equally: Hao-Xin Liu, Shan-Qing Li. ✉email: cma@hnu.edu.cn; jjacj@sdu.edu.cn

Supported metal catalysts have been widely used in the industrial catalysis process because of their adequate active sites and high atom utilization^{1–5}. Recently, nanoengineering has been widely applied on the preparation of solid catalysts with a homogeneous surface structure by anchoring active metal on stable supports^{6,7}. Maintaining the uniformity and high dispersion of the active metal sites has been considered to be the key to the excellent activity of catalysts⁸. However, with the sintering of catalysts, the active metal tends to agglomerate especially under the reaction conditions of high temperature and reducing atmosphere, leading to the serious deactivation^{9,10}. Reducing the loading of the active metal can partly overcome the aggregation, however, the activity of the catalyst is commonly unsatisfactory due to the insufficient active metal sites¹¹. Thus, the construction of stabilized and adequate active sites in the sintered catalyst is a great challenge but also full of significance.

The reverse water gas shift (RWGS) reaction is recognized a most promising way to utilize CO₂, thanks to its high selectivity and low operation pressure^{12–15}. The resulting CO is considered as feedstock to produce various value-add chemicals via Fischer-Tropsch synthesis or other syngas process^{16–18}. Due to its endothermic property, a high working temperature is usually required to facilitate the equilibrium conversion of CO₂. However, it brings huge difficulty to the durability of the catalysts under such harsh conditions^{14,19,20}. Noble metal catalysts, such as Pd- and Pt- based catalysts^{11,21,22}, have been studied for this reaction, however, their practical applications are limited by the inferior catalytic performance and high cost. Among the non-noble metal catalysts, Cu-based catalyst has been considered as the ideal candidate for this reaction because of the high activity, selectivity, and low cost^{13,14,23,24}. However, on one hand, the catalysts with high copper loading are apt to agglomeration, causing severe deactivation²⁴. On the other hand, the low copper loading on supports can partly resist aggregation, but suffers from insufficient active sites and poor catalytic performance⁷. As a result, the conflict between high activity and high stability under harsh reaction conditions limits the development and application of Cu-based catalysts. According to the previous work, ceria (CeO₂) is often recognized as a suitable supports to anchor copper because of the strong interaction between copper and ceria. Using the interaction, the copper-ceria catalyst has shown its unique value in a variety of catalytic reactions, such as low-temperature water-gas shift reaction^{25,26}, CO oxidation²⁷, and CO₂ hydrogenation^{23,28}. Besides, CeO₂ tends to sintered after high-temperature aging, resulting in a dramatic structural transformation²⁹. Recently, our group has constructed stable and atomically dispersed copper site with unsaturated coordination in the sintered copper-ceria catalyst with very low Cu loading of 1 wt% by air-calcination at 800 °C, which exhibited very high and stable activity for CO oxidation²⁷. However, during the long-term harsh reaction conditions of high temperature and reductive atmosphere, the structure of the copper-ceria catalyst is still unclear, especially for the catalyst with relative high copper loading, which undoubtedly limits the development and application of the copper-ceria catalyst.

Herein, we report a partially sintered Cu/CeO₂ catalyst with Cu loading up to 15 wt.% which exhibits extraordinarily high activity and stability for the RWGS reaction under very harsh conditions (600 °C, space velocity of 400,000 mL·g_{cat}⁻¹·h⁻¹). Two-dimensional (2D) and three-dimensional (3D) copper clusters are formed and firmly anchored on the surface of ceria under the reaction conditions due to the interaction between copper and ceria, through which abundant stable active sites were constructed. Further, structural characterization and DFT calculations confirmed that abundant active surface oxygen vacancies were in situ generated and consumed circularly during the reaction, which combined with

adjacent copper clusters to promote the activation of CO₂ and catalytic efficiency. The synergistic catalytic effect of anti-sintering active copper clusters and sufficient surface oxygen vacancies provided a guarantee for the extraordinary activity and stability under harsh conditions. The partially sintered catalyst with excellent catalytic performance breaks the conventional impression that catalysts are severely deactivated upon sintering and shows great potential in the utilization of CO₂.

Results

Catalytic performance in the RWGS reaction. The catalytic performance in the RWGS reaction over various catalysts was evaluated at various temperatures under a high space velocity of 400,000 mL·g_{cat}⁻¹·h⁻¹. As shown in Fig. 1a, the CeO₂ support itself showed very poor catalytic activity. When the reaction temperature reached 600 °C, CO₂ conversion was only 8%. While, after depositing copper on ceria, the catalyst significantly promoted the catalytic activity. The catalytic activity increased with the increasing of copper loading until the copper loading reached 15 wt.% (Supplementary Fig. 1). Among all the prepared catalysts, the 15CuCe catalyst showed the best activity of 146.6 mol_{CO₂}·g_{cat}⁻¹·s⁻¹ at 600 °C, which was at least three times higher than all the other reported catalysts. In addition, the reaction rate of 15CuCe was as high as 52.2 mol_{CO₂}·g_{cat}⁻¹·s⁻¹ at 500 °C, more than one order of magnitude than that of other reported non-noble metal catalysts and even noble metal catalysts (Fig. 1b and Table 1). And it is worth noting that these Cu catalysts show 100% selectivity of CO with no CH₄ detected in the products (Supplementary Fig. 1b). Besides, the catalytic performances of the 15CuCe catalyst under other reaction atmospheres with different H₂:CO₂ ratios were also evaluated. As shown in Supplementary Fig. 2, the CO₂ conversion increased with the increasing of the H₂:CO₂ ratio. And at all these H₂:CO₂ ratios, the 15CuCe catalyst shown excellent catalytic activity, suggesting this catalyst had high catalytic efficiency over a wide range of H₂:CO₂ ratios. And it was noteworthy that even when the H₂:CO₂ ratio reached 4:1, no CH₄ was detected in the production, which indicated the catalyst catalyzed the RWGS reaction much rather than the methanation. To the best of our knowledge, the excellent activity of the 15CuCe catalyst at high temperature is unmatched. As shown in Fig. 1c and Supplementary Fig. 3, the apparent activation energy *E_a* of the 5CuCe catalyst (62.88 kJ·mol⁻¹) and the 15CuCe catalyst (57.92 kJ·mol⁻¹) was much lower than that of the 15CuAl catalyst (133.96 kJ·mol⁻¹). Besides, the 15CuCe catalyst synthesized with CeO₂ nanorod as support exhibited much better activity than that of the 15CuCe-NC and 15CuCe-NP catalysts, indicating the morphologies of CeO₂ supports had important effect on the catalytic performance (Supplementary Fig. 4).

Long-term evaluation of the copper-ceria catalysts was conducted. As illustrated in Fig. 1d, both the 5CuCe and 15CuCe catalyst showed excellent stability. For the 5CuCe catalyst and the 15CuCe catalyst, even under the very harsh condition (600 °C, GHSV = 400,000 mL·g_{cat}⁻¹·h⁻¹), it maintained more than 85% of its initial activity after 70 h test. The activity of both the 5CuCe and the 15CuCe catalysts decreased gradually in the first 20 h and then stabilized. In order to explore the stability of the 15CuCe catalyst further, the test time was extended to 240 h, and the 15CuCe catalyst still showed excellent stability. However, the 15CuCe-NP catalyst with more severe sintering (Supplementary Table 1) showed worse stability and lower activity in the 40 h test (Supplementary Fig. 5). And the reference 15CuAl catalyst lost more than 50% of its original activity within 10 h under the same test conditions. In addition, the reaction rate of the 15CuCe catalyst decreased slightly after six rounds of start-up cool-down stability tests (Supplementary Fig. 6). From the above results, the

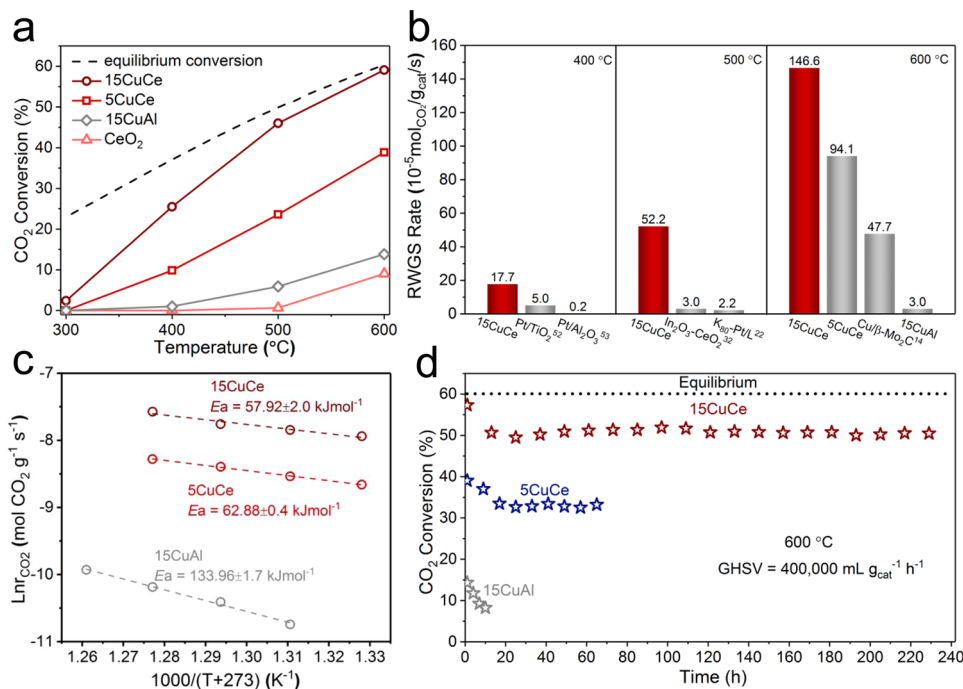


Fig. 1 Catalytic performance of copper–ceria catalysts in RWGS reaction. **a** Activities of CeO₂, 5CuCe, 15CuCe, and 15CuAl catalysts; **b** Comparison of reaction rates for different catalysts at 400 °C, 500 °C, and 600 °C; **c** Apparent activation energy value of various catalysts; **d** Long-term catalytic tests of the 5CuCe, 15CuCe catalysts and the reference 15CuAl catalyst.

Table 1 Comparison of CO₂ Conversion Rate and CO Selectivity for the as-prepared and Literature Reported catalysts.

Catalyst	H ₂ :CO ₂	Temperature (°C)	Pressure (MPa)	Rate (10 ⁻⁵ molCO ₂ /g _{cat} /s)	CO selectivity (%)	Ref
15CuCe	3:1	600	0.1	146.6	100	this work
15CuAl	3:1	600	0.1	3.0	100	this work
Cu/CeO ₂ -hs	3:1	600	0.1	42.5	100	46
4Cu–Al ₂ O ₃	2:1	600	0.1	17.9	100	13
Cu/β–Mo ₂ C	2:1	600	0.1	47.7	99.2	14
Cu-Fe/SiO ₂	1:1	600	0.1	11.9	100	20
NiCe/Zr	3:1	550	0.1	33.3	99.5	48
15CuCe	3:1	500	0.1	52.2	100	this work
In ₂ O ₃ –CeO ₂	1:1	500	0.1	2.98	100	49
K ₈₀ –Pt/L	1:1	500	0.1	2.22	100	22
Ni–in–Cu	3:1	500	0.1	3.95	100	50
CuSiO/CuO _x	3:1	500	0.1	3.18	100	51
TiO ₂ /Cu	3:1	500	0.1	1.78	N/A	51
SiO ₂ /Cu	3:1	500	0.1	1.11	N/A	51
Cu–Zn–Al	2:1	500	0.1	26.1	100	14
Cu/β–Mo ₂ C	2:1	500	0.1	37.9	99.0	14
Pt/TiO ₂	1:1	400	0.1	5.0	100	52
Pt/Al ₂ O ₃	1.4:1	400	N/A	0.16	N/A	53
Ni/Mg(Al)O	3:1	450	0.1	0.5	66.7	54
Fe–CeO ₂	4:1	400	0.1	0.65	100	55

optimal 15CuCe catalyst achieved the combination of high activity and high stability.

Structural characterization of the copper–ceria catalysts. The catalytic performances of catalysts are closely related to the structure of the catalyst. The transmission electron microscopy (TEM) images of the fresh 15CuCe catalyst presented the regular rod-like structure with length ranging from about 50 to 200 nm (Supplementary Fig. 7a). The EDS mapping results (Supplementary Fig. 7b) suggested that copper species were well dispersed in the fresh 15CuCe catalyst. The catalysts with relative

low copper loading exhibited the similar size and morphology as the 15CuCe catalyst (Supplementary Fig. 8). As for the fresh and used 25CuCe catalysts, a large number of isolated copper particles (tens to hundreds nanometers, labeled by circle in red) were observed (Supplementary Fig. 8h and k), which indicated that the optimized copper loading was around 15 wt.%. This phenomenon showed that it was crucial to load proper amount of copper on the ceria support. The addition of excess copper results in agglomeration and deactivation, while catalysts with low Cu concentration suffer from insufficient Cu active sites, ending up with poor catalytic performance. For the 15CuCe catalyst after H₂ pretreatment, the high-angle annular dark-field (HAADF) images

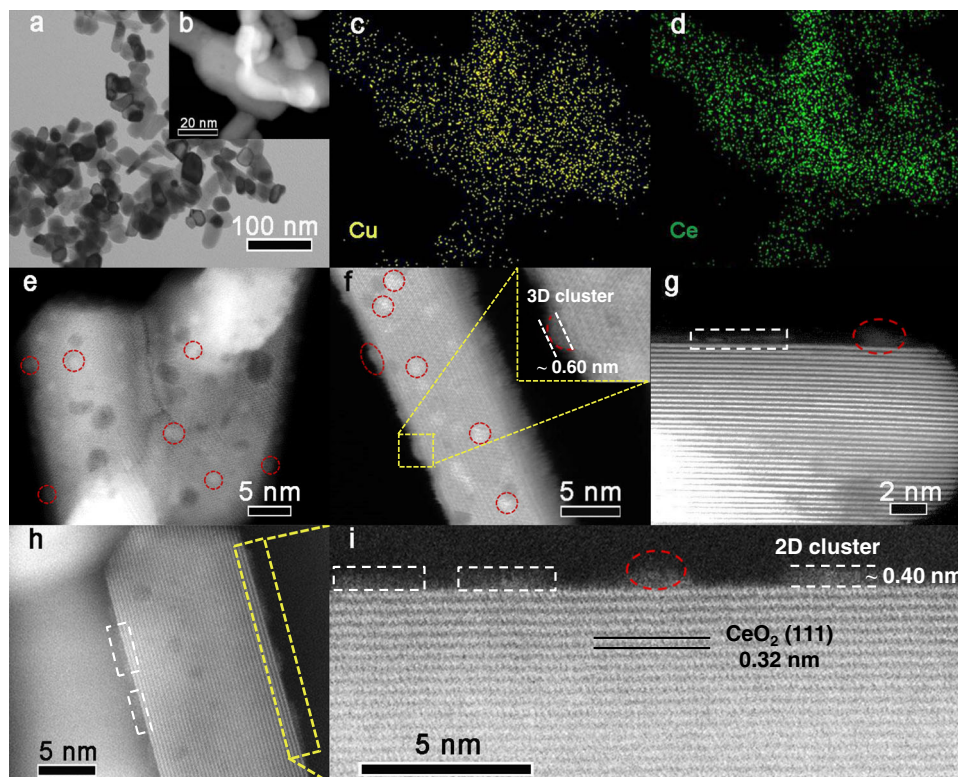


Fig. 2 Structure characterization of the 15CuCe catalyst after 70 h stability test. **a** Transmission electron microscope (TEM) image; **b–d** Scanning transmission electron microscope (STEM) image and element mapping results; **e–h** High-angle annular dark-field (HAADF) STEM images; **i** Enlarged image of the highlighted region in **(h)**.

(Supplementary Fig. 9) indicated that ceria nanorods could maintain the rod-like morphology, suggesting ceria nanorods have not undergone obvious sintering prior to the RWGS reaction. In addition, 2D layered and 3D hemisphere-shaped copper clusters could be clearly observed on the surface of CeO₂ nanorods. The width of the 2D layered clusters ranged from 1 nm to 3.5 nm, and the thickness was from about 0.2 nm to 0.5 nm. The diameter of 3D clusters was around 2 nm. Besides, as shown in Fig. 2a, compared to the used catalyst with slight sintering after temperature-dependent evaluation (Supplementary Fig. 8j), the CeO₂ nanorods underwent more obvious sintering during the long-term reaction of 70 h at high temperature. However, the excellent activity and stability of the catalyst (Fig. 1a and d) meant that there might still be abundant active metal sites on the partially sintered ceria support. As shown in Fig. 2b–d and Supplementary Fig. 10, the EDS elemental mapping images demonstrated the high dispersion of copper, with Cu signal appearing uniformly on the surface of the partially sintered catalyst. And the HAADF images indicated on the surface of the partially sintered copper-ceria catalyst, copper also existed dominantly in the forms of 2D layered clusters and 3D hemisphere shaped clusters (Fig. 2e–i and Supplementary Fig. 11), similar to the activated samples. The average thickness of the layered clusters was about 0.4 nm (Fig. 2i), which was approximately consistent with a bilayer configuration of copper atoms²⁵. The widths of the 2D layered clusters varied from 1.5 nm to 4 nm. And the mean width and average thickness of the 3D clusters were 1.3 nm and 0.6 nm, respectively.

Although many excellent reports have explored the structure of copper-ceria catalysts^{25,27}, the structure of the copper-ceria catalyst, including the status of copper species and morphology of ceria, is almost unknown under harsh reaction conditions (at high temperature and with the reductive atmosphere), especially

for the catalyst with relatively high copper loading. In order to explore the structure of the 15CuCe catalyst after a long enough reaction time, the measurement by an HAADF-STEM of the sample after 240 h RWGS reaction was performed. As shown in Fig. 3a, CeO₂ nanorods were still partially sintered, but not completely sintered, which indicated that CeO₂ nanorods could not oversinter to cause the severe deactivation. And the EDS mapping images (Fig. 3b–d and Supplementary Fig. 12) suggested that the copper species were still highly dispersed on the partially sintered CeO₂ support. As illustrated in Fig. 3e–i, even though the reaction time has been extended to 240 h, 2D and 3D copper clusters were anchored on the partially sintered CeO₂ nanorods, which undoubtedly prevented the catalyst from being inactivated by the agglomeration of active copper species. According to the above experimental results, the structural evaluation of the 15CuCe catalyst during the long-term reaction could be shown in the Fig. 3j. Under the harsh reaction conditions, the ceria support sintered partially, but copper species were still anchored as clusters on the catalyst surface. However, for the reference 15CuAl catalyst, even though the Al₂O₃ support was very stable under high temperature, copper species have agglomerated significantly during the reaction, which caused severe deactivation in activity (Supplementary Fig. 13). And the 15CuCe catalyst prepared by the impregnation (IMP) method with poor dispersion of copper also exhibited much inferior activity (Supplementary Fig. 14).

In Table 2, the actual Cu content of the copper-ceria catalysts was similar to that of the theoretical value. And the Cu/CeO₂ catalysts exhibited similar specific BET surface areas (80.1–88.2 m²·g⁻¹) except the 15CuAl catalyst showed a larger value 154.7 m²·g⁻¹. X-ray diffraction (XRD) results (Supplementary Fig. 15) showed that fluorite CeO₂ served as dominate phase for all the fresh and used catalysts except the 25CuCe catalyst. And from the XRD results

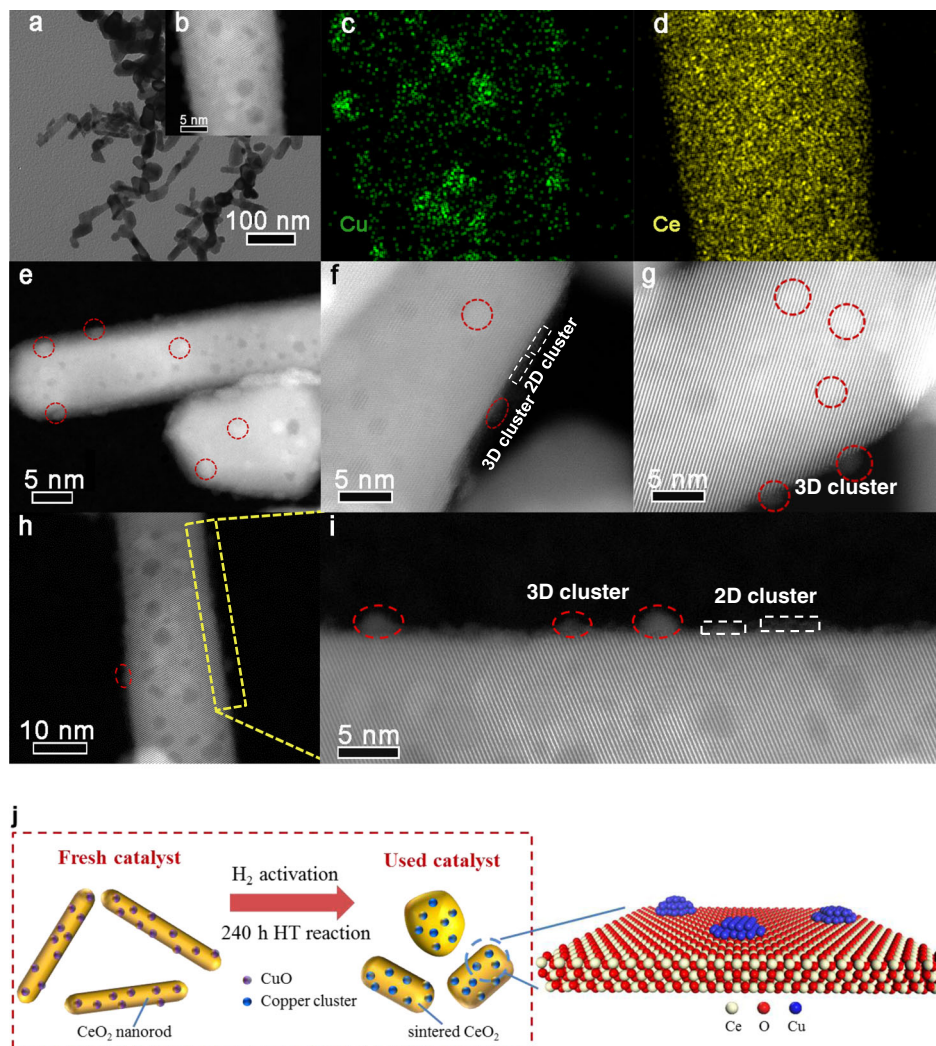


Fig. 3 Structure characterization of the 15CuCe catalyst after 240 h stability test. **a** TEM image; **b–d** STEM images and element mapping results. **e–h** HAADF-STEM images; **i** Enlarged image of the highlighted region in **(h)**; **j** Scheme of structural evolution for the copper–ceria catalyst during long-term stability test.

Table 2 Physicochemical properties of catalysts.

Catalyst	Cu (wt.%) ^a	S _{BET} (m ² ·g ⁻¹) ^b	H ₂ (μmol·g ⁻¹) ^c	Integral D/F _{2g} signal ^d
1CuCe	0.8	86.2	α430, β124	α0.11, β0.16
5CuCe	3.4	88.2	α1191, β510	α0.47, β0.67
10CuCe	9.7	83.9	α2543, β1352	α0.60, β0.96
15CuCe	15.2	83.3	α3791, β1996	α0.65, β1.50
25CuCe	26.5	80.1	α4647, β3062	α0.75, β1.69
15CuAl	16.1	154.7	/	/

^aDetermined with ICP-OES.

^bDetermined with N₂ adsorption.

^cActual values of H₂ consumption (α) and theoretic values of H₂ consumption calculated according to Cu²⁺ → Cu⁰ (β).

^dD/F_{2g} internal ratio of fresh catalysts (α) and used catalysts (β).

(Supplementary Fig. 13) of the fresh 15CuCe and used 15CuCe catalysts after 70 h stability test, it could be seen that copper species existed mainly in the form of CuO before the reaction and metallic Cu⁰ after the reaction. The tiny diffraction peak of Cu⁰ also suggested that copper could maintain very small size even after a long period of high-temperature reaction, which was also consistent with the results of STEM. The Cu 2*p* X-ray photoelectron spectroscopy (XPS) spectra of the fresh, activated, and used 15CuCe catalyst were shown in Supplementary Fig. 16. The XPS peaks centered at 933.6 and 932.4 eV were attributed to the Cu 2*p*_{3/2}

region; According to the previous reports, the peak centered at 933.6 eV was attributed to the Cu²⁺ species, and 932.4 eV was assigned to Cu⁺/Cu⁰ species³⁰. It indicated that only Cu²⁺ was detected for the fresh 15CuCe catalyst, while for the activated and used 15CuCe sample, the Cu⁺/Cu⁰ species appeared. This result indicated that the surface Cu²⁺ species was reduced to Cu⁺ or Cu⁰ in the activation process.

The interaction between the copper and ceria in the catalyst.

The high dispersion of the copper species reflected the interaction between copper and ceria. For the fresh Cu/CeO₂ catalysts, such interaction can be confirmed by H₂ temperature-programmed reduction (H₂-TPR)⁸. As shown in supplementary Fig. 17a, the TPR profiles could be deconvoluted into three peaks. In the previous report³¹, the EXAFS data confirmed the existence of Cu-O and Cu-Ce binding in the Cu/CeO₂-NR catalyst, which was quite consistent with the reduction peaks of CuO_x clusters and the Cu-[O_x]-Ce structure. However, the experimental result in the Supplementary Fig. 17b and other reports³² indicated that the H₂-TPR pattern of pure CuO was not completely symmetric, which suggested that the reduction of CuO_x was not completed in one step, suggesting the CuO_x species were progressively reduced to Cu⁺ and Cu⁰ species. Besides, the reduction peak of CuO

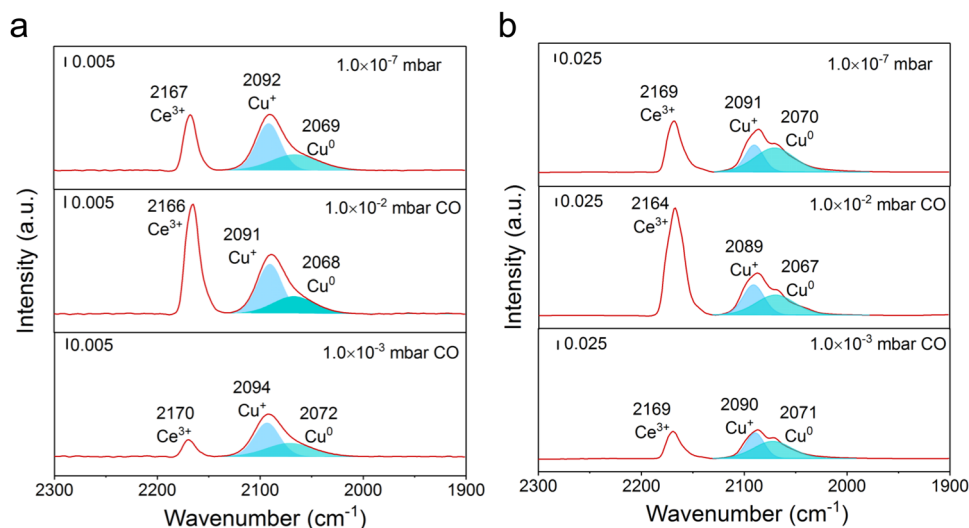


Fig. 4 The interaction between copper and ceria. **a–b** In situ infrared spectra recorded after exposing the 15CuCe catalyst to CO with different partially pressure at $-143\text{ }^{\circ}\text{C}$ after H_2 pretreatment (**a**) and 70 h stability test at $600\text{ }^{\circ}\text{C}$ (**b**), respectively.

could not be deconvoluted into two symmetric peaks, indicated the reduction of Cu^{2+} to Cu^+ and the reduction of Cu^+ to Cu^0 occurred simultaneously in a certain range of reduction temperature. Therefore, we speculated the reduction peaks of highly dispersed CuO_x clusters in copper-ceria catalysts were also not symmetric, and the α and β peaks could not be attributed to the reduction of single species, but the progressively reduction of CuO_x species to Cu^+ and Cu^0 species. Furthermore, the high-temperature sharp peak ($170\text{--}260\text{ }^{\circ}\text{C}$) was due to the reduction of the strong interaction of $\text{Cu}\text{--}[\text{O}_x]\text{--}\text{Ce}$ structure³⁰. Comparing to the H_2 -TPR results of pure CeO_2 and CuO (Supplementary Fig. 17b), the $\text{CuO}\text{--}\text{CeO}_2$ interaction enhanced the redox properties of these catalysts³³. However, the reduction temperature of the reference 15CuAl catalyst was close to that of pure CuO , which meant there was a very weak interaction between copper and alumina (Supplementary Fig. 18). With such weak interaction, copper were difficult to be stabilized on the Al_2O_3 support under the high-temperature reduction conditions, causing the severe deactivation of the 15CuAl catalyst.

In order to further explore the interaction between the interfacial copper and ceria in the 15CuCe catalyst after the H_2 pretreatment and the stability test, the in situ infrared spectroscopy at the low temperature ($-143\text{ }^{\circ}\text{C}$) was measured by using the CO as probe molecule. As shown in Fig. 4a, three CO bands appeared after 1.0×10^{-3} mbar CO was injected. The band at $2166\text{--}2170\text{ cm}^{-1}$ was assigned to CO adsorbed at the Ce^{3+} site²⁵. And the two bands at 2092 cm^{-1} and 2069 cm^{-1} were attributed to the CO adsorption on the Cu^+ and Cu^0 sites³⁴, respectively. The intensity of all CO bands increased with the increase of CO pressure, especially at the Ce^{3+} site. Then with the rising of the degree of vacuum to 1.0×10^{-7} mbar, the rapid elimination of adsorbed CO at the Ce^{3+} was observed, which was related to the weak binding energy of $\text{CO}\text{--}\text{Ce}^{3+}$. The $\text{CO}\text{--}\text{Cu}^+$ related infrared bands demonstrated that part of Cu^+ sites could not be reduced during the H_2 activation process. Besides, as for the partially sintered 15CuCe sample after the stability test, there were also three bands appeared (Fig. 4b). The presence of the Cu^+ site and the Ce^{3+} site confirmed that the interaction between the positively charged copper atoms with electrophilicity and the Ce^{3+} with nucleophilicity was not destroyed after long time treatment of reductive atmosphere at high temperature of $600\text{ }^{\circ}\text{C}$. The H_2 -TPR result for the 15CuCe catalyst after the temperature-programmed surface reaction (TPSR) test also gave a reduction

peak (Supplementary Fig. 19), which again suggested a part of copper species remain $\text{Cu}^{\delta+}$ with electrophilicity during the reaction due to the interaction between copper and ceria³². Therefore, there was no doubt that the stable interaction between copper and ceria were present, which ensured the high dispersion and high stability of the active copper sites under harsh conditions.

Role of the surface oxygen vacancy in the catalysts. Due to the interaction between copper and ceria, the Ce^{4+} can be transformed to Ce^{3+} , which is accompanied by the formation of oxygen vacancy^{8,34–36}. It has been reported that oxygen vacancies commonly are recognized as the crucial active site to adsorb and dissociate CO_2 ^{28,37}, playing an important role in the CO_2 reduction reaction. Luis F. Bobadilla et al. demonstrated that the dissociation paths of CO_2 on reductive and non-reductive supports could activate CO_2 more efficiently³⁸. However, CO_2 is a stable molecule, whose dissociation rate is closely related to the number of oxygen vacancies³⁹. In this work, ex situ and in situ Raman spectra were performed to characterize the oxygen vacancies of the catalysts. In ex situ Raman results of all fresh and used copper-ceria catalysts (Supplementary Fig. 20), besides the vibration mode (F_{2g}) of CeO_2 fluorite-type structure at $\sim 454\text{ cm}^{-1}$, a broad D band was also found⁸. The D_1 peak located at $\sim 543\text{ cm}^{-1}$ resulted from surface oxygen vacancy where Ce^{4+} was replaced by Ce^{3+} . And the D_2 peak at $\sim 603\text{ cm}^{-1}$ was the intrinsic defect in ceria^{40,41}. The relative integral intensity ratio of D/F_{2g} reflected the concentration of oxygen vacancies in each catalyst^{3,8,42,43}. As illustrated in Supplementary Figure 20, the relative strength of the D band gradually increased with the increase of copper loading which meant that copper could promote the creation of oxygen vacancies. And the oxygen vacancy concentration of the used catalysts was higher (Table 2), indicating that more oxygen vacancies were created during the pretreatment and reaction process. The H_2 -TPR results of all the Cu/CeO_2 catalysts also reflected that the amounts of hydrogen consumption of these catalysts were bigger than the theoretical values based on the complete reduction of Cu^{2+} to Cu^0 (Table 2). This was due to the reduction of surface oxygen of the ceria at relatively low temperature by the aids of highly dispersed copper clusters. The more practical H_2 consumption exceeded the theoretical value, the more

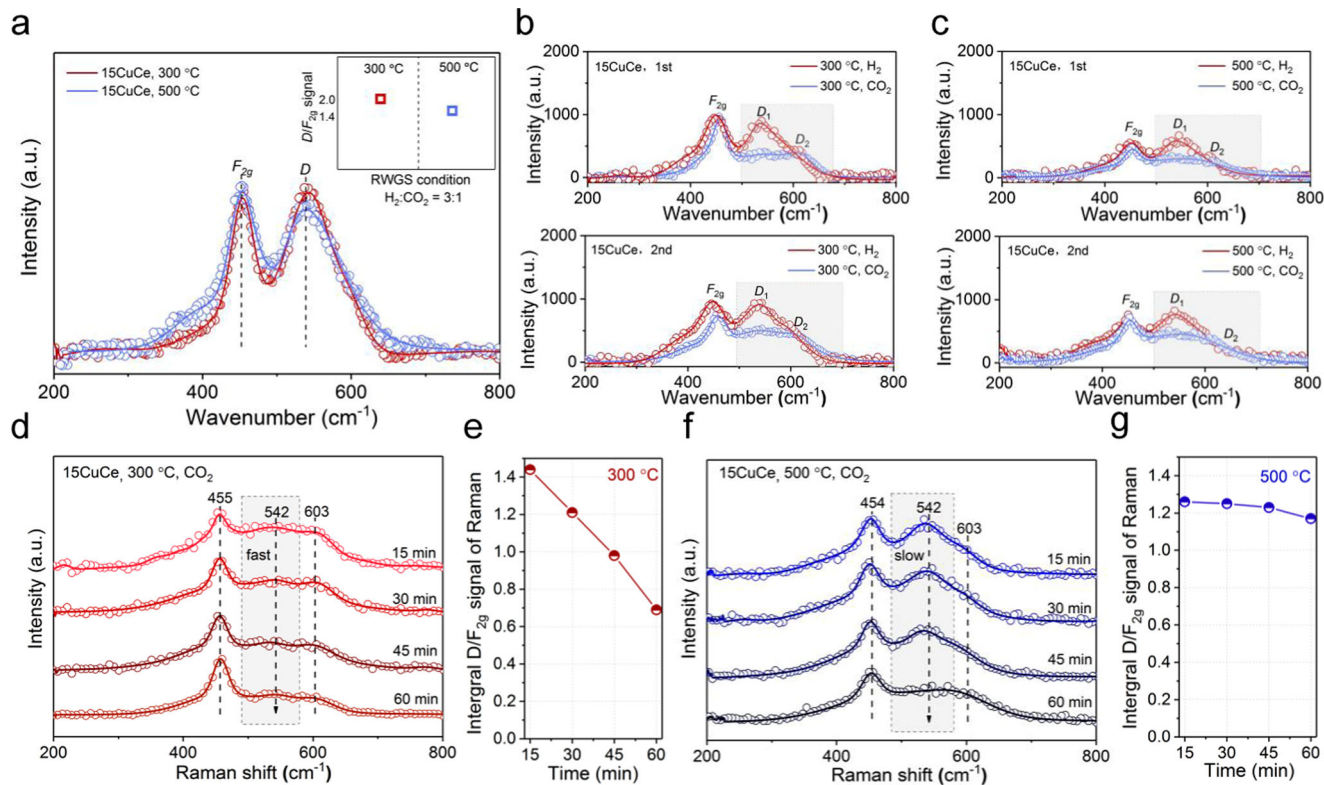


Fig. 5 Examination of oxygen vacancies in the copper-ceria catalysts. **a** In situ Raman under the RWGS reaction conditions for the 15CuCe catalyst; **b–c** In situ Raman of the 15CuCe catalyst with H₂/CO₂ switching under 300 °C and 500 °C, respectively; **d–e** The in situ Raman spectra over the 15CuCe catalyst under CO₂ flow at 300 °C and the variation of $I_D/I_{F_{2g}}$ intensity ratio with time; **f–g** The in situ Raman spectra over the 15CuCe catalyst under CO₂ flow at 500 °C and the variation of $I_D/I_{F_{2g}}$ intensity ratio with time.

oxygen vacancies were formed⁴⁴. And for the Cu/CeO₂ catalysts after reaction, more oxygen vacancies were produced on the surface by the effect of the reductive reaction gas (69% H₂/23% CO₂/ 8% N₂).

To explore the role of oxygen vacancy in the actual reaction process further, the in situ Raman under reaction condition at 300 °C and 500 °C were measured and the results were showed in Fig. 5a. The 15CuCe catalyst showed a strong peak centered at 543 cm⁻¹, which was assigned as surface oxygen vacancies. Compared to the fresh 15CuCe catalyst, the D₁ band was even pronounced than F_{2g} peak during the reaction process, which meant that abundant surface oxygen vacancies were in situ generated during the reaction process. For the 5CuCe catalyst, the D₁ band was also obvious, which meant surface oxygen vacancies were ubiquitous in the reaction process for Cu/CeO₂ catalysts in this work (Supplementary Fig. 21). And as exhibited by the illustrations in Fig. 4a and Supplementary Fig. 21, the in situ Raman tests reflected that the copper-ceria catalyst contained similar concentrations of oxygen vacancies at 300 °C and 500 °C. The small difference in the concentration of the oxygen vacancy could be considered within the error range. Besides, for the pure CeO₂ support (Supplementary Fig. 22), the intensity of the D peak was very weak in the reaction atmosphere, which again demonstrated that the addition of copper could create more oxygen vacancies on the surface of ceria.

In order to explore the relationship between the activation of reactant molecules (H₂ and CO₂) and the oxygen vacancy, the in situ Raman spectra of the 15CuCe catalyst with CO₂/H₂ switch under 300 °C and 500 °C were also measured. As shown in the Fig. 5b and c, the Raman spectra of the 15CuCe catalyst after H₂ treatment showed a strong characteristic peak of oxygen surface vacancy centered at 543 cm⁻¹. When CO₂ was filled in, the

intensity of D₁ peak diminished, which meant that CO₂ adsorbed on the surface oxygen vacancies and occupied them. However, the stable D₂ peak suggested that CO₂ adsorption almost has little effect on the intrinsic defects. This experimental phenomenon directly confirmed that the surface oxygen vacancy was involved in this reaction. The second cycle of in situ Raman measurement also gave the same conclusion that surface oxygen vacancies were created by H₂, and consumed by CO₂. This in situ Raman result indicated that the surface oxygen vacancies could be consumed and regenerated as the reaction progress, allowing for the existence of lots of surface oxygen vacancies on the catalyst surface which could promote the high activity and stability. Besides, the relationship between the concentration of oxygen vacancy and CO₂ treatment time at 300 °C and 500 °C was also explored. As shown in the Fig. 5d–g, the decrease rate of oxygen vacancy at 300 °C was significantly faster than that at 500 °C. Combined with the results of the CO₂-TPD in Supplementary Fig. 23, the adsorption of CO₂ became more and more difficult with the increase of temperature. Therefore, it was easier for CO₂ to adsorb on oxygen vacancies at 300 °C compared to 500 °C. Besides, the effects of H₂ and CO₂ concentrations on the oxygen vacancy have also been investigated. As shown in Supplementary Fig. 24, the addition of CO₂ could reduce the amount of oxygen vacancies. However, further increasing the concentration of CO₂ did not significantly reduce the concentration of oxygen vacancies, which suggested that the rate, which CO₂ consume oxygen vacancies was much slower than the rate of which H₂ produced oxygen vacancies. The rapid formation of oxygen vacancies also meant the 15CuCe catalyst with dispersed copper clusters has a strong ability to dissociate H₂.

Meanwhile, as illustrated in Supplementary Fig. 25, the reaction orders of CO₂ for the 15CuCe and 5CuCe catalysts

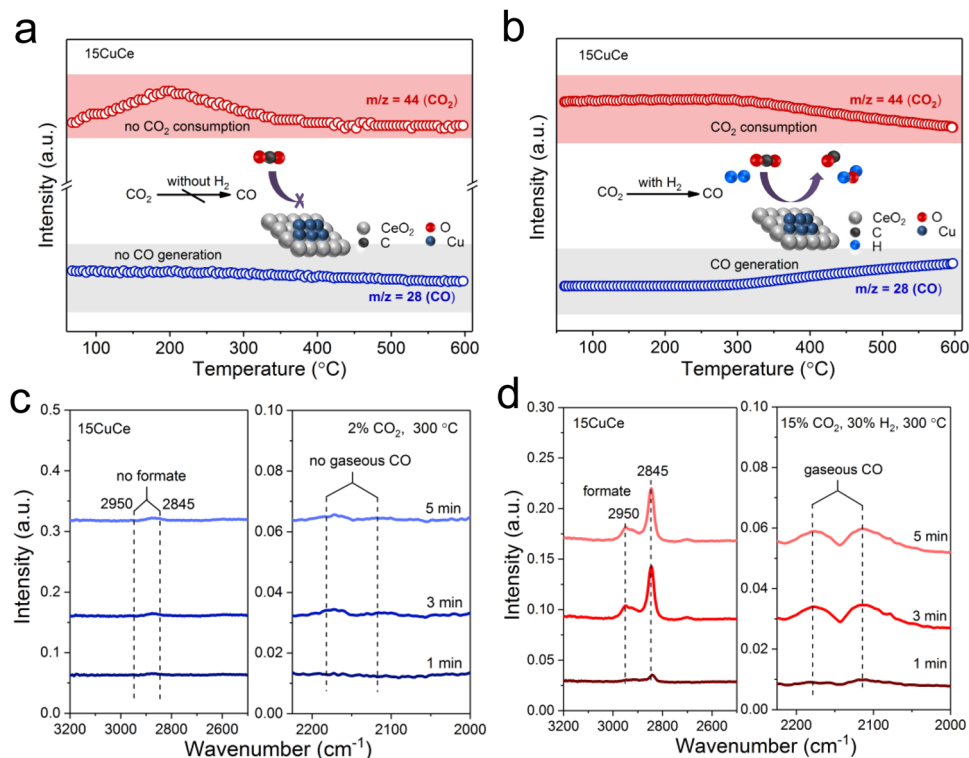


Fig. 6 RWGS mechanism and reactive intermediates study of the 15CuCe catalyst. **a** The CO₂ dissociation experiment of the 15CuCe catalyst; **b** TPRS results of the 15CuCe catalyst; **c–d** In situ diffused reflectance infrared Fourier transform spectroscopy (DRIFTS) spectra of 15CuCe catalyst during CO₂ treatment and reaction conditions at 300 °C, respectively.

were 0.25 and 0.52, respectively. And the reaction orders of H₂ over the 15CuCe and 5CuCe catalysts were 0.25 and 0.3, respectively. The lower apparent reaction orders of CO₂ and H₂ on the 15CuCe catalyst compared to the 5CuCe sample reflected the reaction rate on the 15CuCe catalyst was less dependent on the concentrations of CO₂ and H₂, which might suggested CO₂ and H₂ were relatively easily adsorbed on the 15CuCe catalyst with more oxygen vacancies and copper sites.

Reaction mechanism study. The mechanisms of the RWGS reaction have been classified into two categories, redox mechanism, and associative mechanism¹⁹. Whether the dissociated H species involve in the formation of reactive intermediates (such as formate) is the key to distinguish these two mechanisms⁴⁵. In this work, the dissociation experiment of CO₂ was performed to probe the reaction pathway. After the catalyst pretreated by H₂/Ar at 600 °C for 1 h, the CO₂/Ar mixed gas was introduced into the reactor at room temperature. As shown in Fig. 6a, there was no consumption of CO₂ except for a part of the desorbed CO₂ during the adsorption process. Meanwhile, there was no generation of CO could be found. The above experimental results indicated that it was difficult for CO₂ itself to be directly dissociated to form CO by the 15CuCe catalyst. In Fig. 6b, the TPRS result illustrated that CO₂ signal gradually decreased and CO signal gradually increased from ~300 °C, suggesting CO₂ was converted into CO with the assistance of H₂. Thus, combing the results of CO₂ dissociation experiment and TPRS, it could be concluded that CO₂ activation may processed via an associative intermediate pathway.

To further explore the active intermediates, the in situ diffused reflectance infrared Fourier transform spectroscopy (DRIFTS) was carried out. As shown in the Fig. 6c and Supplementary Fig. 26a, after the injection of CO₂, only carbonate signal appeared and no CO gas signal was generated, which indicated

carbonate was hard to dissociate directly into CO. However, as shown in Fig. 6d and Supplementary Fig. 26b, after the injection of CO₂ and H₂ over the activated 15CuCe catalyst, in addition to the carbonate signal, the C=O vibration peak of formate at 1373 cm⁻¹ and the typical C-H stretch vibration peaks of formate at 2949 cm⁻¹ and 2845 cm⁻¹ were observed^{46,47}. Simultaneously, the broadband, which was attributed to the gaseous CO at 2000–2200 cm⁻¹ has been detected as the increasing of the formate signal.

Calculations based on density functional theory (DFT) were also performed. The adsorption characteristics of CO₂ suggested that the presence of Cu atoms assured that the decreasing entropy step could occur, shown as Fig. 7a, b and Supplementary Table 2. Notwithstanding the situation of oxygen vacancy affected the binding force, the energy could be reduced more than one electron-volt under the bonding interaction between Cu and CO₂. And in the presence of H₂, Cu atoms captured H₂ molecule and broken H-H bond, then transferred H atom to CO₂, shown as Fig. 7c. Formate structures formed accompanying the formation of C-H bond, and these structures exhibited in the intermediate IMA3, IMA3-I, IMA4, and IMA4-I. The heat liberation declared that the formate formation was a thermodynamic feasible elementary reaction. The subsequent hydrogen-migration step ($\Delta E = 1.587$ eV) was the thermodynamically limiting step, and this might be the reason that formate signals were detected by DRIFTS. Carboxylic intermediates, IMA3-II and IMA4-II, were involved in the mechanism at the same time. Different from the formate intermediates, one step was absent from the carboxylic path, i.e., IMA4-II produced IMA6 directly. Based on the above experimental results and DFT calculations, we could further infer that the associative mechanism was involved in this reaction and the surface formate and carboxylic species might be the important reactive intermediates. The synergistic catalytic effect between copper clusters and oxygen vacancies copper clusters promoted

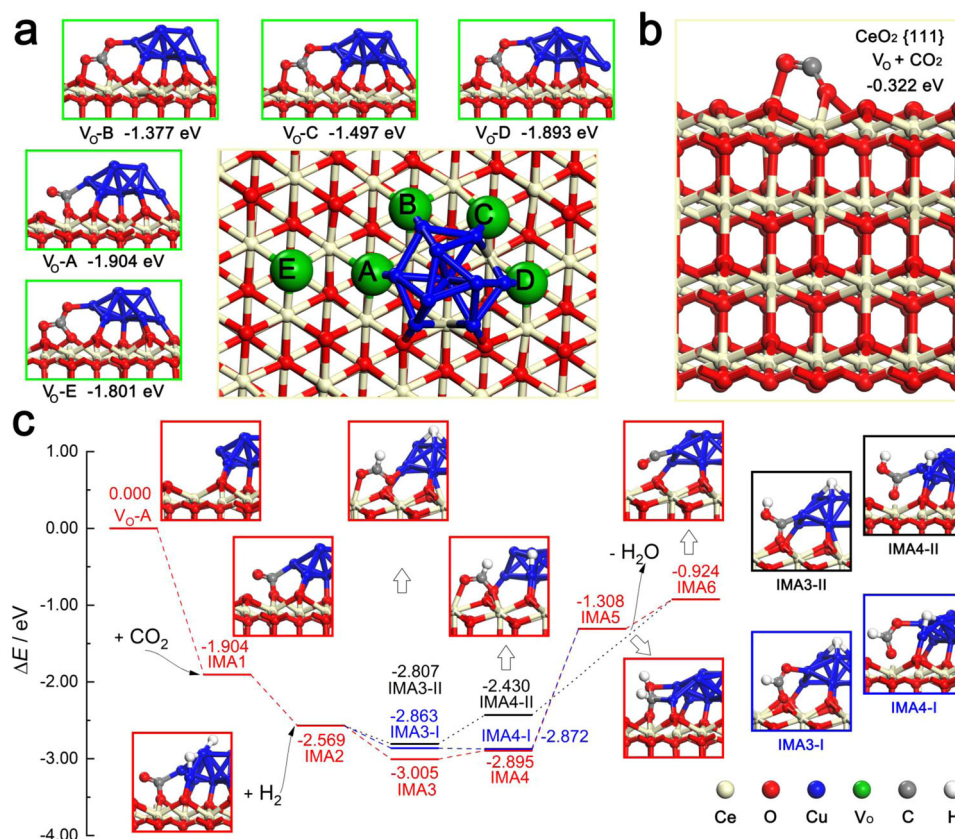


Fig. 7 The proposed reaction pathways for the RWGS reaction on the copper–ceria catalyst. **a** Chemisorption of CO₂ on the 10Cu/CeO₂{111} surface. Five oxygen vacancies, named after V_O-A to V_O-E, were made comparisons, and the selected CO₂ was located close to V_O-A; **b** The adsorption energy that CO₂ was bound to V_O on the CeO₂{111} surface was obviously weaker than those of Cu dropped ceria sites; **c** RWGS reaction mechanism occurred in the V_O-A. The red, blue, and black lines indicated different reaction paths, and the structural diagrams with the red, blue or black stroke corresponded to the reaction paths, respectively.

the adsorption of CO₂ and the formation of active intermediates. The sufficient copper clusters and abundant oxygen vacancies in the 15CuCe catalyst undoubtedly created more metal cluster-oxygen vacancy active interfaces.

Discussion

For high-temperature catalytic reactions, the development of catalysts with both high activity and excellent stability has always been difficult. In this work, highly dispersed active copper clusters with high loading (15 wt.%) were stably constructed on the partially sintered copper-ceria catalyst during the real reaction process. The optimal 15CuCe catalyst exhibited excellent catalytic performance to catalyze the RWGS reaction at high operating temperature, which surpassed almost all the reported non-noble metal catalysts and costly noble metal catalysts. The harsh reaction conditions of high temperature and reductive atmosphere caused the ceria support sintered partially, while the interaction between copper and ceria maintained well. The unexpected stable interaction ensured the copper species to maintain stable in the forms of 2D layered clusters and 3D hemisphere-shaped clusters on the partially sintered ceria support. Besides, abundant surface oxygen vacancies were in situ generated and consumed circularly during the reaction process, forming the synergistic catalytic effect with copper cluster to promote the activation of CO₂ and the formation of active intermediates. The unmatched activity and solid stability of this catalyst show great potentials in the practical applications. And the reveal of the structure-function relationship of the catalyst with sintered configuration also provides a reference for other systems.

Methods

Preparation of copper–ceria catalysts. The copper-ceria catalyst was prepared by the deposition-precipitation (DP) method. Firstly, the ceria support (0.50 g) was dispersed in 30 mL high purity water under continuous stirring. Next, different amounts of copper precursor, Cu(NO₃)·3H₂O, were dissolved in 12.5 mL of high pure water, and then added into the above CeO₂/H₂O suspension dropwise. During the process of instilling, the pH value of the solution was controlled to ca. 9 by adding Na₂CO₃ solution (0.50 mol·L⁻¹). The obtained precipitates were further aged at room temperature for 1 h before filtration, followed by washing with high pure water (1 L) at room temperature. The resulting material was dried in air at 75 °C overnight and then calcined in still air at 600 °C for 4 h (heating rate: 2 °C/min). The copper-ceria samples synthesized in this work were denoted as xCuCe (x = 1, 5, 10, 15 and 25), where x is the copper content in weight percent (x = [Cu/CeO₂]/wt × 100%). The reference copper-ceria catalyst was prepared using the impregnation (IMP) method. 0.5 g of CeO₂ support was dispersed in deionized water by stirring. Then the suitable amount of copper nitrate was added into the slurry. The obtained mixture was dried at 90 °C using an oil bath under stirring. The resulting material was calcined in still air at 600 °C for 4 h (heating rate: 2 °C/min). The reference copper-ceria sample was denoted as 15CuCe-IMP.

Transmission electron microscopy (TEM). Transmission electron microscopy (TEM) was undertaken by JEM-2100F (JEOL) instrument operating at 200 kV. The samples were dispersed in ethanol by ultrasonic and dropped on the carbon-coated Cu grid before test. The images of high-resolution TEM (HR-TEM) were obtained by using a JEOL JEM-2800 instrument with an acceleration voltage of 200 kV. The element mapping results and EDS analysis were acquired from the same machine under STEM mode. The High-angle annular dark-field scanning transmission electron microscopy (HAADF-STEM) images were obtained on a Thermo Scientific Themis Z microscope equipped with a probe-forming spherical-aberration corrector.

Raman test. All the ex situ and in situ Raman spectra were acquired by using a Raman microscope system (HORIBA JY) with laser excitation at 633 nm. The integration times of ex situ and in situ Raman spectra were 1 min and 5 min, respectively.

In situ infrared spectroscopy in the transmission mode. The infrared measurements were conducted in a UHV apparatus combining a FTIR spectrometer (Bruker Vertex 70 v) with a multi-chamber UHV system. The sample was pre-treated with H₂ or reaction gas at 873 K for 30 min, and then exposed to CO with desired pressure at 130 K.

Catalytic tests and kinetics measurement. The catalytic performance evaluation was tested in a fixed-bed flow reactor under a gas atmosphere of 23% CO₂/69% H₂/N₂ (66.7 mL·min⁻¹, Deyang Gas Company, Jinan) at 1 bar total pressure. Before the activity test, 10 mg catalysts (40–60 mesh) diluted with 90 mg inert SiO₂ were activated by 5% H₂/Ar at 600 °C for 60 min followed by switching to the feed gas for testing. The test temperature ranges from 300 °C to 600 °C. And before the analysis of gas products, the RWGS reaction needs to stabilize for 60 min at each test temperature. The gas products were analyzed by using an on-line gas chromatograph equipped with a thermal conductivity detector (TCD). CO₂ conversion and CO selectivity were calculated using the following equations:

$$X_{\text{CO}_2} = \frac{n_{\text{CO}_2}^{\text{in}} - n_{\text{CO}_2}^{\text{out}}}{n_{\text{CO}_2}^{\text{in}}} \times 100 \quad (1)$$

$$S_{\text{CO}} = \frac{n_{\text{CO}}^{\text{out}}}{n_{\text{CO}}^{\text{out}} + n_{\text{CH}_4}^{\text{out}}} \times 100 \quad (2)$$

where $n_{\text{CO}_2}^{\text{in}}$ is the concentration of CO₂ in the reaction stream, and $n_{\text{CO}_2}^{\text{out}}$, $n_{\text{CO}}^{\text{out}}$, $n_{\text{CH}_4}^{\text{out}}$ are the concentrations of CO, CO₂, CH₄ in the outlet. The CO₂ thermodynamic equilibrium conversion was calculated from HSC chemistry software version 6.0. The ratio of H₂:CO₂ in the initial state was 3:1, and the products including CO, H₂O and CH₄ were taken into account in the calculation process. For all catalysts, the E_a was measured by using the same reactor for catalytic performance above. Appropriate amount of catalysts diluted with inlet SiO₂ were used in the kinetics experiments. And in order to obtain accurate kinetics data, the catalysts need to be first treated with reactive gas for an hour at 600 °C. During the kinetic test, the CO₂ conversion remained between 5% and 15% by changing gas flow rate. The reaction orders of CO₂ and H₂ for the catalysts were measured under 500 °C. The RWGS activity was recorded while the concentration of CO₂ or H₂ in the reaction gas was varied on purpose.

Data availability

The main data supporting the findings of this study are available within the article and its Supplementary information. All other relevant source data are available from the corresponding author upon reasonable request. Source data are provided with this paper.

Received: 9 June 2021; Accepted: 3 January 2022;

Published online: 14 February 2022

References

- Zhang, X. et al. A stable low-temperature H₂-production catalyst by crowding Pt on α -MoC. *Nature* **589**, 396–401 (2021).
- Cargnello, M. et al. Control of metal nanocrystal size reveals metal-support interface role for ceria catalysts. *Science* **341**, 771–773 (2013).
- Fu, X. et al. Direct Identification of Active Surface Species for the Water-Gas Shift Reaction on a Gold-Ceria Catalyst. *J. Am. Chem. Soc.* **141**, 4613–4623 (2019).
- Zhang, Z. et al. Intrinsically Active Surface in a Pt/ γ -Mo₂N Catalyst for the Water-Gas Shift Reaction: Molybdenum Nitride or Molybdenum Oxide? *J. Am. Chem. Soc.* **142**, 13362–13371 (2020).
- Qiao, B. et al. Single-atom catalysis of CO oxidation using PtI/FeOx. *Nat. Chem.* **3**, 634–641 (2011).
- Liu, X. et al. Activation of subnanometric Pt on Cu-modified CeO₂ via redox-coupled atomic layer deposition for CO oxidation. *Nat. Commun.* **11**, 4240 (2020).
- Chen, C. S., Lin, J. H., You, J. H. & Chen, C. R. Properties of Cu(thd)₂ as a Precursor to Prepare Cu/SiO₂ Catalyst Using the Atomic Layer Epitaxy Technique. *J. Am. Chem. Soc.* **128**, 15950–15951 (2006).
- Yan, H. et al. Construction of stabilized bulk-nano interfaces for highly promoted inverse CeO₂/Cu catalyst. *Nat. Commun.* **10**, 3470 (2019).
- Campbell, C. T., Parker, S. C. & Starr, D. E. The effect of size-dependent nanoparticle energetics on catalyst sintering. *Science* **298**, 811–814 (2002).
- Dai, Y., Lu, P., Cao, Z., Campbell, C. T. & Xia, Y. The physical chemistry and materials science behind sinter-resistant catalysts. *Chem. Soc. Rev.* **47**, 4314–4331 (2018).
- Nelson, N. C., Chen, L., Meira, D., Kovarik, L. & Szanyi, J. In Situ Dispersion of Palladium on TiO₂ During Reverse Water-Gas Shift Reaction: Formation of Atomically Dispersed Palladium. *Angew. Chem. Int. Ed.* **59**, 17657–17663 (2020).
- Juneau, M. et al. Assessing the viability of K-Mo₂C for reverse water-gas shift scale-up: molecular to laboratory to pilot scale. *Energ. Environ. Sci.* **13**, 2524–2539 (2020).
- Bahmanpour, A. M. et al. Cu-Al Spinel as a Highly Active and Stable Catalyst for the Reverse Water Gas Shift Reaction. *ACS Catal.* **9**, 6243–6251 (2019).
- Zhang, X. et al. Highly Dispersed Copper over β -Mo₂C as an Efficient and Stable Catalyst for the Reverse Water Gas Shift (RWGS) Reaction. *ACS Catal.* **7**, 912–918 (2016).
- Zhang, Q., Pastor-Pérez, L., Jin, W., Gu, S. & Reina, T. R. Understanding the promoter effect of Cu and Cs over highly effective β -Mo₂C catalysts for the reverse water-gas shift reaction. *Appl. Catal. B: Environ.* **244**, 889–898 (2019).
- Fu, X. et al. Co₃O₄-Al₂O₃ mesoporous hollow spheres as efficient catalyst for Fischer-Tropsch synthesis. *Appl. Catal. B: Environ.* **211**, 176–187 (2017).
- Ashwell, A. P. et al. Hydrogenation of CO to Methanol on Ni(110) through Subsurface Hydrogen. *J. Am. Chem. Soc.* **139**, 17582–17589 (2017).
- Williamson, D. L., Herdes, C., Torrente-Murciano, L., Jones, M. D. & Mattia, D. N-Doped Fe@CNT for Combined RWGS/FT CO₂ Hydrogenation. *ACS Sustain. Chem. Eng.* **7**, 7395–7402 (2019).
- Su, X., Yang, X., Zhao, B. & Huang, Y. Designing of highly selective and high-temperature durable RWGS heterogeneous catalysts: recent advances and the future directions. *J. Energy Chem.* **26**, 854–867 (2017).
- Chen, C. Study of iron-promoted Cu/SiO₂ catalyst on high temperature reverse water gas shift reaction. *Appl. Catal. A: General.* **257**, 97–106 (2004).
- Zhao, Z. et al. Atomically dispersed Pt/CeO₂ catalyst with superior CO selectivity in reverse water gas shift reaction. *Appl. Catal. B: Environ.* **291**, 120101 (2021).
- Yang, X. et al. Promotion effects of potassium on the activity and selectivity of Pt/zeolite catalysts for reverse water gas shift reaction. *Appl. Catal. B: Environ.* **216**, 95–105 (2017).
- Ronda-Lloret, M., Rico-Francés, S., Sepúlveda-Escribano, A. & Ramos-Fernandez, E. V. CuO_x/CeO₂ catalyst derived from metal organic framework for reverse water-gas shift reaction. *Appl. Catal. A: General.* **562**, 28–36 (2018).
- Vovchok, D. et al. Deciphering Dynamic Structural and Mechanistic Complexity in Cu/CeO₂/ZSM-5 Catalysts for the Reverse Water-Gas Shift Reaction. *ACS Catal.* **10**, 10216–10228 (2020).
- Chen, A. et al. Structure of the catalytically active copper-ceria interfacial perimeter. *Nat. Catal.* **2**, 334–341 (2019).
- Si, R. et al. Structure sensitivity of the low-temperature water-gas shift reaction on Cu-CeO₂ catalysts. *Catal. Today* **180**, 68–80 (2012).
- Yu, W. et al. Construction of Active Site in a Sintered Copper-Ceria Nanorod Catalyst. *J. Am. Chem. Soc.* **141**, 17548–17557 (2019).
- Yang, S. et al. Synergy between Ceria Oxygen Vacancies and Cu Nanoparticles Facilitates the Catalytic Conversion of CO₂ to CO under Mild Conditions. *ACS Catal.* **8**, 12056–12066 (2018).
- Aneggi, E., Wiater, D., de Leitenburg, C., Llorca, J. & Trovarelli, A. Shape-Dependent Activity of Ceria in Soot Combustion. *ACS Catal.* **4**, 172–181 (2013).
- Wang, W. et al. Highly Dispersed Copper Oxide Clusters as Active Species in Copper-Ceria Catalyst for Preferential Oxidation of Carbon Monoxide. *ACS Catal.* **5**, 2088–2099 (2015).
- Wang, W. et al. Crystal Plane Effect of Ceria on Supported Copper Oxide Cluster Catalyst for CO Oxidation: Importance of Metal-Support Interaction. *ACS Catal.* **7**, 1313–1329 (2017).
- Yan, H. et al. Promoted Cu-Fe₃O₄ catalysts for low-temperature water gas shift reaction: Optimization of Cu content. *Appl. Catal. B: Environ.* **226**, 182–193 (2018).
- Sripada, P. et al. Investigating the dynamic structural changes on Cu/CeO₂ catalysts observed during CO₂ hydrogenation. *J. Catal.* **381**, 415–426 (2020).
- Kang, L. et al. The Electrophilicity of Surface Carbon Species in the Redox Reactions of CuO-CeO₂ Catalysts. *Angew. Chem. Int. Ed.* **60**, 14420–14428 (2021).
- Elias, J. S. et al. Elucidating the Nature of the Active Phase in Copper/Ceria Catalysts for CO Oxidation. *ACS Catal.* **6**, 1675–1679 (2016).
- Kang, L. et al. Adsorption and activation of molecular oxygen over atomic copper(I/II) site on ceria. *Nat. Commun.* **11**, 4008 (2020).
- Geng, Z. et al. Oxygen Vacancies in ZnO Nanosheets Enhance CO₂ Electrochemical Reduction to CO. *Angew. Chem. Int. Ed.* **57**, 6054–6059 (2018).
- Bobadilla, L. F., Santos, J. L., Ivanova, S., Odriozola, J. A. & Urakawa, A. Unravelling the Role of Oxygen Vacancies in the Mechanism of the Reverse Water-Gas Shift Reaction by Operando DRIFTS and Ultraviolet-Visible Spectroscopy. *ACS Catal.* **8**, 7455–7467 (2018).
- Yang, S. et al. Oxygen Vacancy Engineering of Cerium Oxides for Carbon Dioxide Capture and Reduction. *ChemSusChem* **6**, 1326–1329 (2013).
- Vindigni, F., Manzoli, M., Damin, A., Tabakova, T. & Zecchina, A. Surface and Inner Defects in Au/CeO₂ WGS Catalysts: Relation between Raman Properties, Reactivity and Morphology. *Chem.- A Eur. J.* **17**, 4356–4361 (2011).

41. Wu, Z., Li, M., Howe, J., Meyer, H. M. & Overbury, S. H. Probing Defect Sites on CeO₂ Nanocrystals with Well-Defined Surface Planes by Raman Spectroscopy and O₂ Adsorption†. *Langmuir* **26**, 16595–16606 (2010).
42. Wang, H. et al. Roles of oxygen vacancy and O⁻ in oxidation reactions over CeO₂ and Ag/CeO₂ nanorod model catalysts. *J. Catal.* **368**, 365–378 (2018).
43. Huang, W. & Gao, Y. Morphology-dependent surface chemistry and catalysis of CeO₂ nanocrystals. *Catal. Sci. Technol.* **4**, 3772–3784 (2014).
44. Dai, B., Cao, S., Xie, H., Zhou, G. & Chen, S. Reduction of CO₂ to CO via reverse water-gas shift reaction over CeO₂ catalyst. *Korean. J. Chem. Eng.* **35**, 421–427 (2018).
45. Chen, X. et al. Identification of relevant active sites and a mechanism study for reverse water gas shift reaction over Pt/CeO₂ catalysts. *J. Energy Chem.* **25**, 1051–1057 (2016).
46. Zhang, Y. et al. Highly efficient Cu/CeO₂-hollow nanospheres catalyst for the reverse water-gas shift reaction: Investigation on the role of oxygen vacancies through in situ UV-Raman and DRIFTS. *Appl. Surf. Sci.* **516**, 146035 (2020).
47. Zhang, X. et al. Synergy between β-Mo₂C Nanorods and Non-thermal Plasma for Selective CO₂ Reduction to CO. *Chem* **6**, 3312–3328 (2020).
48. Zonetti, P. C. et al. The Ni_xCe_{0.75}Zr_{0.25-x}O₂ solid solution and the RWGS. *Appl. Catal. A: General.* **475**, 48–54 (2014).
49. Wang, W. et al. Reverse water gas shift over In₂O₃-CeO₂ catalysts. *Catal. Today* **259**, 402–408 (2016).
50. Wang, L. et al. Dispersed Nickel Boosts Catalysis by Copper in CO₂ Hydrogenation. *ACS Catal.* **10**, 9261–9270 (2020).
51. Yu, Y. et al. Highly active and stable copper catalysts derived from copper silicate double-shell nanofibers with strong metal-support interactions for the RWGS reaction. *Chem. Commun.* **55**, 4178–4181 (2019).
52. Chen, X. et al. Catalytic performance of the Pt/TiO₂ catalysts in reverse water gas shift reaction: Controlled product selectivity and a mechanism study. *Catal. Today* **281**, 312–318 (2017).
53. Kim, S. S., Lee, H. H. & Hong, S. C. A study on the effect of support's reducibility on the reverse water-gas shift reaction over Pt catalysts. *Appl. Catal. A: General.* **423–424**, 100–107 (2012).
54. Rodrigues, M. T. et al. RWGS reaction employing Ni/Mg(Al,Ni)O—The role of the O vacancies. *Appl. Catal. A: General.* **543**, 98–103 (2017).
55. Xiong, K. et al. CO₂ Reverse Water-Gas Shift Reaction on Mesoporous M-CeO₂ Catalysts. *Can. J. Chem. Eng.* **95**, 634–642 (2017).

Acknowledgements

This work was financially supported from the National Science Foundation of China (Grant No. 21771117, 21805167, 22075166), the Taishan Scholar Project of Shandong Province of China, the Young Scholars Program of Shandong University (Grant No. 11190089964158), the Outstanding Youth Scientist Foundation of Hunan Province (Grant No. 2020JJ2001), and the Key Project of Educational

Department of Anhui Province (Grant No. KJ2019A0861). We thank the Center of Structural Characterizations and Property Measurements at Shandong University for the help on sample characterizations.

Author contributions

C.J.J. and C.M. supervised the work; H.X.L. and C.J.J. designed the experiments, analyzed the results and wrote the manuscript; S.Q.L. made the DFT calculations; H.X.L. and W.W.W. performed the in situ DRIFTS, in situ Raman; H.X.L. and W.Z.Y. performed the catalysts preparation, catalytic tests and the TPR tests; W.J.Z. and C.M. performed the aberration-corrected HAADF-STEM measurements and analyzed the results.

Competing interests

The authors declare no competing interests.

Additional information

Supplementary information The online version contains supplementary material available at <https://doi.org/10.1038/s41467-022-28476-5>.

Correspondence and requests for materials should be addressed to Chao Ma or Chun-Jiang Jia.

Peer review information *Nature Communications* thanks the anonymous reviewers for their contribution to the peer review of this work. Peer reviewer reports are available.

Reprints and permission information is available at <http://www.nature.com/reprints>

Publisher's note Springer Nature remains neutral with regard to jurisdictional claims in published maps and institutional affiliations.



Open Access This article is licensed under a Creative Commons Attribution 4.0 International License, which permits use, sharing, adaptation, distribution and reproduction in any medium or format, as long as you give appropriate credit to the original author(s) and the source, provide a link to the Creative Commons license, and indicate if changes were made. The images or other third party material in this article are included in the article's Creative Commons license, unless indicated otherwise in a credit line to the material. If material is not included in the article's Creative Commons license and your intended use is not permitted by statutory regulation or exceeds the permitted use, you will need to obtain permission directly from the copyright holder. To view a copy of this license, visit <http://creativecommons.org/licenses/by/4.0/>.

© The Author(s) 2022